H2S removal by copper enriched porous carbon cuboids

Thomou, Eleni; Basina, Georgia; Spyrou, Konstantinos; Wahedi, Yasser Al; Rudolf, Petra; Gournis, Dimitrios

Published in:
Carbon Trends

DOI:
10.1016/j.cartre.2022.100145

Publication date:
2022

Carbon Trends 7 (2022) 100145

Contents lists available at ScienceDirect

Carbon Trends

journal homepage: www.elsevier.com/locate/cartre

H_2S removal by copper enriched porous carbon cuboids

Eleni Thomou[a,b], Georgia Basina[c], Konstantinos Spyrou[a], Yasser Al Wahedi[c,*], Petra Rudolf[b,*], Dimitrios Gournis[a,**]

[a] Department of Materials Science and Engineering, University of Ioannina, Ioannina, GR 45110, Greece
[b] Zernike Institute for Advanced Materials, University of Groningen, Groningen, AG 9747, the Netherlands
[c] Department of Chemical Engineering, Khalifa University, Sas Al Nakhl Campus, P.O. Box 2533, Abu Dhabi, United Arab Emirates

ARTICLE INFO

Article history:
Received 30 August 2021
Revised 6 December 2021
Accepted 2 January 2022

Keywords:
Carbon cuboids
Porous sorbent
Adsorption
Catalysis
Selective oxidation H_2S

ABSTRACT

Hydrogen sulfide (H_2S) removal by adsorption from gas streams is crucial to prevent the environmental and industrial damage it causes. Amongst the nanostructures considered excellent candidates as sorbents, porous carbon has been studied extensively over the last years. In the present work we present a synthetic procedure for three high potential sorbents based on carbon cuboids, namely a low-surface-area copper-rich structure, a highly porous aggregate without metal addition, and lastly the same porous carbon decorated with copper. The properties and performance as catalysts of these three sorbents were evaluated by powder X-ray diffraction, X-ray photoelectron spectroscopy, thermal analysis, scanning electron microscopy with energy dispersive X-ray analysis, surface area determination through N_2 adsorption and desorption, as well as by H_2S adsorption measurements.

1. Introduction

Hydrogen sulfide (H_2S), is a hazardous, colourless, flammable gas, with a 'rotten egg' odour, that can be encountered either in the natural environment of gas/crude oil wells and hot springs, or as a by-product of industrial activities [1]. It has lethal effects on humans and animals and at the same time is the cause for extreme corrosion in industrial facilities [2]. A lot of effort has been put into developing technologies that can effectively remove H_2S and mitigate its negative effects; most of them fall under the following categories: absorption, adsorption, conversion, catalytic reactions, chemical oxidation, chemical scrubbing, incineration, and biological treatment [1–4].

Adsorption is the most widely applied approach due to the good balance between cost and effectiveness [1], and amongst the types of sorbents that have been studied for capturing H_2S (activated carbons, zeolites, polymers, metal oxides, *etc.*)[5–8], porous carbons are particularly attractive due to their surface chemistry and large surface areas [3,9,10]. Furthermore, it has been proven that the desulfurization performance can be further improved when combining a porous matrix, that acts as support, with metal oxides [11–14]. Apart from adsorption, both carbon-based materials and metal oxides are being successfully used in desulfurization processes that involve catalytic procedures [15–21].

Inspiration for the present work came from a recently reported new member of the carbon family that combines porosity with the capability to accept functional groups on its surface, and has shown excellent performance in the capture of atmospheric water vapour [22]. This novel nanostructure is called porous carbon cuboids (PCCs) and combines a series of intriguing properties, such as light weight, unusual ultra-hydrophilic behaviour, great stability, surface heterogeneity, and a very high hierarchical porosity (estimated approximately 800-900 m^2/gr) [22]. In contrast to graphene, which has to be subjected to oxidation in order to make it easily processible in solution, PCCs are highly hydrophilic as synthesized because of the high number of functional groups on the surface. PCCs show a significant number of N:C and O:C active sites, which, in combination with the narrow micropore size distribution, promote adsorption. Additionally, they have the advantage of being functional up to 400 °C and can therefore be used in higher temperature applications. The specific geometrical characteristics, hierarchical porosity, and surface chemistry identify PCCs as perfect hosts for metallic nanoparticles (NPs) that are homogeneously distributed on their surface as well as inside their pores.

* Corresponding authors.
** Corresponding author at: Department of Materials Science and Engineering, University of Ioannina, Ioannina, GR 45110, Greece.
E-mail addresses: ytm1983@gmail.com (Y.A. Wahedi), p.rudolf@rug.nl (P. Rudolf), dgourni@uoi.gr (D. Gournis).

https://doi.org/10.1016/j.cartre.2022.100145

Immobilizing metal cations *via* functional groups avoids aggregation, which would compromise the outstanding properties of such nanoparticles [23,24]. In fact, PCC scaffolds decorated with Cu and Ag NPs have already been confirmed as promising antibacterial agents [25].

To explore how the high surface area and the presence of copper oxide can be balanced and how they synergistically affect hydrogen sulfide removal, in the study reported here three different carbon nanostructures were synthesized and their performance evaluated with a H_2S chemisorption experiment at 150 °C. Powder X-ray diffraction (XRD), X-ray photoelectron spectroscopy, thermal analysis, scanning electron microscopy (SEM) with energy dispersive X-ray analysis (EDX), as well as surface area determination through N_2 adsorption and desorption were used to characterize the novel sorbents.

1.1. Materials and methods

1.1.1. Materials

4,4′ bipyridine (98%) was purchased from Alfa Aesar, ethanol (absolute, 99.9%) was obtained by J.T. Baker, Pluronic F127 and copper chloride dihydrate (≥ 99%) $CuCl_2 \bullet 2H_2O$ were acquired from Sigma-Aldrich, and nitric acid (> 65%) HNO_3 was purchased from Boom BV. All reagents were of analytical grade and used without further purification. The water used in the experiments was distilled and deionized.

1.1.2. Materials synthesis

PCC synthesis: Two solutions were prepared. The first one consisted of 1 g of pluronic dissolved in 100 mL of 0.1 M 4,4′-bipyridine in water-ethanol (volume ratio of 1:17) and the second one was an aqueous solution of copper (II) chloride (900 mL, 5.6 mM $CuCl_2 \bullet 2H_2O$). The first solution was then poured rapidly into the second one under vigorous stirring. The formed products were retrieved through centrifugation, washed three times with water, and air-dried. The turquoise-coloured product was then pyrolyzed under argon flow (500 °C for 2 h, heating rate 1 °C/min) and the copper species were leached away (stirred in a 4 M HNO_3 aqueous solution for 24 h). The final black powder was washed with water until pH was ∼5.0 and air dried. This sample was denoted as *PCC* [22]. The intermediate product before the leaching step was denoted as *PCC-unleached.*

PCC-Cu synthesis: Metal-substituted porous carbon materials were synthesized using Cu. PCCs were dissolved in a metal salt aqueous solution (approximately 10% w/w). The mixture was stirred for 1 h and then centrifuged. The precipitate was dissolved again in a new solution (1 h stirring), and the material was centrifuged again, washed with water, and air-dried. This sample is denoted as *PCC-Cu*.

1.1.3. Characterization techniques

The XRD patterns of the PCC, PCC-unleached and PCC-Cu were collected on a D8 Advance Bruker diffractometer with a Cu Kα X-ray source (wavelength 1.5418 Å) and a secondary beam graphite monochromator. In the case of PCC-unleached a 1 mm divergent slit and a 3 mm antiscattering slit were used. The patterns were recorded in a 2θ range from 2 to 80 °, in steps of 0.02 ° and with a counting time of 2.00 s per step. The XRD measurements that were recorded before and after the H_2S adsorption measurements, were performed on a Panalytical X'Pert PRO powder diffractometer. About 30 mg of the selected sample was first placed on a zero-background holder and the measurements were conducted using Cu-Kα radiation (λ = 1.5406 Å). The diffraction patterns were collected over the 2θ range of 10 ° to 80 ° with a step size of 0.02 ° and the time per step of 1.3 s. The nitrogen adsorption-desorption isotherms for PCC and PCC-Cu were measured on a Sorptomatic 1990 Thermo Finnigan porosimeter and for PCC-unleached on a Autosorb iQ gas sorption system from Quantachrome Instruments at 77 K. Specific surface area values were determined by the Brunauer–Emmett–Teller (BET) method. The samples were degassed under high vacuum for 10 h at 100 °C prior to the measurements. XPS measurements on the PCC and PCC-Cu were performed under ultra-high vacuum conditions with a base pressure of 5×10^{-10} mbar with a SPECS GmbH instrument equipped with a monochromatic Mg Kα source (hν = 1253.6 eV) and a Phoibos-100 hemispherical analyser. Samples were suspended in water, drop casted on Si wafers, and after drying left in high vacuum overnight to outgas, before being transferred to the main chamber for XPS measurement. The energy resolution was set to 1.18 eV, and the photoelectron take-off angle was 45° with respect to the surface normal. Recorded spectra were the average of three scans with the energy step set to 0.05 eV and a dwell time of 1 s. XPS measurements for PCC-unleached were performed using a Surface Science SSX-100 ESCA instrument with a monochromatic Al Kα X-ray source (hν = 1486.6 eV). The pressure in the measurement chamber was maintained at 1×10^{-9} mbar during data acquisition. The electron take-off angle with respect to the surface normal was 37° The XPS data were acquired by using a spot size of 1000 μm in diameter and the energy resolution was 1.3 eV for both the survey spectra and the detailed spectra of the core level regions. The Au4$f_{7/2}$ core level was used as a reference binding energy [26]. For the measurements, evaporated polycrystalline 150 nm thick gold films supported on mica (grade V-1, TED PELLA), prepared by sublimation of 99.99% gold (Schöne Edelmetaal B.V.) as detailed in Mendoza et al. [27] were used as substrates where freshly prepared samples were drop casted. Deconvolution of the spectra included a Shirley[28] baseline subtraction and peak deconvolution employing mixed Gaussian−Lorentzian functions. All XPS spectra were analysed using the least-squares curve-fitting program Winspec (developed at LISE laboratory of the University of Namur, Belgium). Thermogravimetric (TG) and differential thermal (DTA) analyses were performed using a Perkin Elmer Pyris Diamond TG/DTA and a TA-Instruments Discovery TGA 5500. Samples of approximately 5 mg were heated in air from 25 to 800 °C, at a rate of 5 °C/min. SEM images of PCC and PCC-Cu were recorded using a JEOL instrument (JSM-6510LV with a LaB_6 filament) equipped with an EDS detector (Oxford Instruments, x-act) operating at an accelerating voltage of 20 kV and using high vacuum (10^{-5} bar). All samples were in the form of a powder; they were placed on a double-sided carbon tape and were measured without coating. The SEM images of PCC-unleached were recorded using a Zeiss Gemini 500 Scanning Electron Microscope. The SEM images of the samples before and after the H_2S adsorption measurements were obtained on a Quanta 250 FEG-FEI microscope, using a Schottky field emission gun as the electron source, with a spatial resolution of ∼1 nm at 5–10 kV. Elemental analysis and phase mapping were also conducted using this microscope, equipped with an Apollo silicon drift detector, integrated with the EDAX Genesis software.

1.1.4. H_2S adsorption

Hydrogen sulfide adsorption experiments were performed at atmospheric pressure in a fixed-bed U-shaped quartz reactor with 4 mm internal diameter. After sieving to sizes ranging between 125 μm and 250 μm, 200 mg of quartz particles were used to dilute 10 mg of the sorbent and the mixture was transferred to the reactor, where it was sandwiched between two layers of quartz wool. After pre-treating the bed at 150 °C overnight using a stream of ultra-pure Ar (flow rate: 44 mL/min, 5.0 purity) to remove all water and residues, a feed gas consisting of 100 ppm H_2S in N_2 was introduced at a flow rate of 40.5 mL/min. Effluents of the bed were analysed using a PerkinElmer Clarus 580 gas chromatograph equipped with Model Arnel 4025 PPC and Model Arnel 4016 PPC

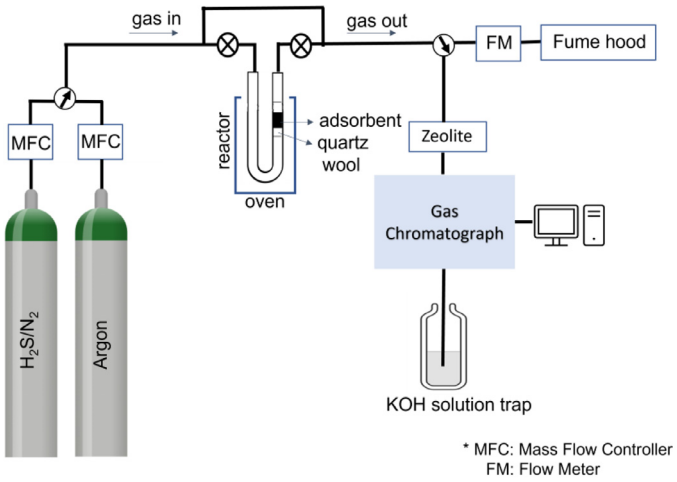

Fig. 1. Schematic diagram of the H_2S breakthrough setup.

sulfur chemiluminescence detector. After breakthrough took place, the argon gas was passed through the system to flush out any remaining H_2S. (The schematic diagram of the H_2S breakthrough setup is shown in Fig. 1)

Sulfur capacity and conversion determination: To determine the sulfur capacity and conversion we proceeded as detailed in refs [29,30]. The breakthrough time was determined as the time when the total concentration of sulfur gases (H_2S+SO_2) at the outlet exceeded 5 ppm and the experiment was stopped at 100 ppm of H_2S at the outlet [11]. The sulfur capacity (mmol/g) was calculated from the Eq. (1), defined as the total H_2S moles adsorbed per mass of sorbent.

$$Sulfur\ capacity\left(\frac{mmol}{g}\right) = \frac{Total\ moles\ adsorbed\ of\ H_2S}{Mass\ of\ sorbent\ (g)} \times 10^{-3} \quad (1)$$

The total moles of H_2S adsorbed was estimated taking into consideration the amount of H_2S (mol/s) passing through the reactor and the breakthrough time as:

$$Total\ moles\ adsorbed\ of\ H_2S\ (mol) = \int_0^{t_{bt}} (\dot{n}_{in} - \dot{n}_{out})dt \quad (2)$$

$$\dot{n} = \frac{xP\dot{V}}{RT} \quad (3)$$

where $\dot{n}_{in}$ is H_2S molar rate in the bed effluent (mol/s), t_{bt} is the breakthrough time, x is H_2S mole fraction either in the feed gas or in the bed effluent, $\dot{V}$ is the feed gas volumetric flow rate at standard conditions (L/s), P is pressure (kPa), R the universal gas constant ($L{\cdot}kPa{\cdot}K^{-1}{\cdot}mol^{-1}$) and T the temperature (K).

The sorbent utilization can be calculated as follows:

$$Utilization = \frac{Sulfur\ capacity}{12.571 Y_{CuO}} \quad (4)$$

where: 12.571 is the maximum theoretical capacity of CuO in mmols of H_2S per gram CuO, Y_{CuO} is the mass fraction of CuO in the sample.

Hydrogen sulfide conversion was calculated at 1000 min on stream as follows:

$$H_2S\ Conversion = \frac{\dot{n}_{in} - \dot{n}_{out} - \dot{n}_{SO2}}{\dot{n}_{in}} \quad (5)$$

where $\dot{n}_{in}$ is the H_2S molar rate in the feed gas (mol/s), $\dot{n}_{out}$ is the H_2S molar rate in the bed effluent (mol/s), and $\dot{n}_{SO2}$ is the molar flow rate of SO_2 in the bed effluent (mol/s) [31].

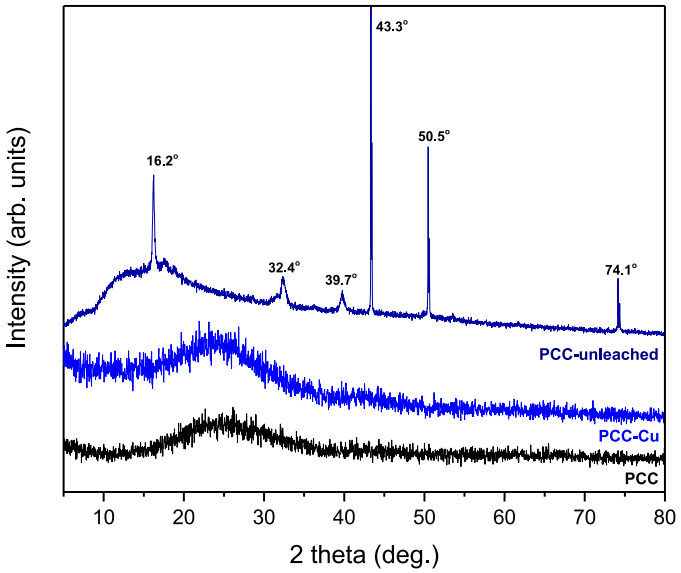

Fig. 2. XRD patterns of PCC-unleached, PCC-Cu and PCC.

2. Results and discussion

2.1. Structural and morphological characterization of the sorbents

In order to verify that the synthesis of the porous carbon cuboids was successful and their properties the same as reported in literature[22], we applied a series of characterization techniques as detailed in the following.

The pore characteristics of PCC, PCC-Cu, and PCC-unleached were investigated by nitrogen adsorption and desorption analysis. The corresponding isotherms are presented in Fig. S1. By applying the Brunner-Emmett-Teller theory, we found that PCC shows a high apparent surface area of ~824 m^2/g, which is in agreement with the first carbon cuboids reported [22] and with our earlier batches [25,32]. After the addition of copper the apparent surface area of PCC-Cu is slightly lower than that of the pristine compound (BET_{SA} ~790 m^2/g). As expected, due to the high amount of copper present in PCC-unleached the porosity is significantly lower with an apparent surface area of 245 m^2/g.

The X-ray diffraction patterns of all three samples are shown in Fig. 2. The patterns for PCC and PCC-Cu are similar, both exhibiting only one broad peak at ~25° that is characteristic of an amorphous structure. The absence of sharp peaks in the case of PCC-Cu is attributed to the good distribution of the copper species as well as the fact that the broad carbon peak is superimposed to and probably covering the copper peaks. On the contrary, in the XRD pattern of the PCC-unleached six peaks appear at 16.2°, 32.4°, 39.7°, 43.3°, 50.5° and 74.1°, which, considering their FWHM (full width at half maximum) and shape, can be divided into groups that correspond to different crystal structures containing copper. Three phases were identified: metallic Cu (sharp double peaks at 43.3°, 50.5° and 74.1°) [33], CuO (32.4° and 39.7°) [33] and $CuCl_2$ (16.2°) [34,35].

Thermogravimetric (TG) analysis was performed on pure carbon cuboids as shown in Fig. 3. The TG curve testifies to the total absence of copper traces (within the detection limit) after the synthetic preparation of PCC. From the TG curves of PCC-Cu and PCC-unleached, we calculated that the metal NPs embedded in the final nanostructure make up 4.5 wt.% of PCC-Cu, while for PCC-unleached the metal remaining at the end of the heat treatment corresponds to 65 wt.%.

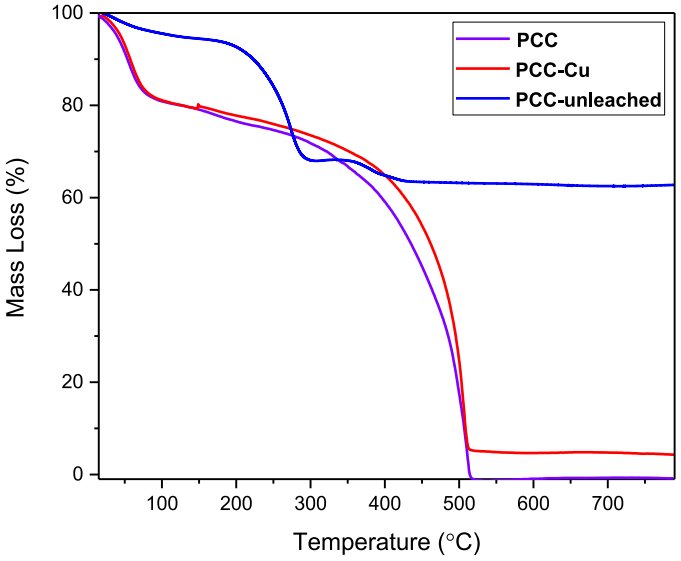

Fig. 3. Thermogravimetric analyses of PCC, PCC-Cu and PCC-unleached.

The morphology of the samples was characterized with SEM. The image in Fig. 4 top left shows the typical cubic structure of PCCs, where randomly aggregated particles overlap with each other. One also notices that the surface of the particles is not smooth but shows many macroporous holes, analogously to what has been observed in previous reports [22,25]. As seen in Fig. 4 top right, this distinctive shape of the nanomaterial is already formed before the leaching step, with the only difference being that much of the mass of PCC-unleached is made up by copper. The morphology of PCC-Cu, whose image is presented in Fig. 4 bottom, remained almost unaffected by the metal substitution.

XPS provides insight in the elemental composition, and the chemical environment of the elements. Fig. 5 shows the XPS spectrum of the C1*s* core level region of PCC; five contributions are necessary to obtain a good fit. The intense peak at a binding energy (BE) of 284.6 eV is due to C − C bonds and accounts for 51.6% of the total C1*s* spectral intensity, whereas the contribution at 285.8 eV is attributed to C − O and C − N moieties, which represent 27.9% of the total amount of carbon. The peaks at BEs of 287.4 and 289.1 eV are attributed to C = O and carboxylic groups, respectively. Finally, the fifth peak, located at 291.1 eV, is a shake-up satellite, characteristic of the aromatic structures [36].

In the case of PCC-Cu, the decoration with copper was confirmed by the detection of a Cu2*p* core level photoemission signal (see Fig. 6). Unfortunately, the amount of copper is so small that the low intensity of the signal does not allow to extract more information than that the copper is in the form of oxides.

In the survey scan of PCC-unleached, presented in Fig. 7(a), we find the signature of the expected elements, namely carbon, oxygen, nitrogen, chlorine and copper, and by analysing the detailed spectra of the various core level regions we can calculate the atomic composition as C 44.1 at.%, O 32.4 at.%, N 11.8 at.%, Cl 7.5 at.% and Cu 4.1 at.%. The large Au4*f* signature and the other Au peaks arise from the Au/mica substrate on which the sample was deposited.

The XPS spectrum of the C1*s* core level region, shown in Fig. 7(b), requires seven contributions to obtain a good fit. The first peak at a BE of 284.2 eV derives from C–Cu bonds, the most intense peak at 285.0 eV is due to the C–C bond, whereas the one at 286.1 eV is attributed to the C–O and C–N bonds [36]. The peaks at 287.3 and 288.6 eV arise from the C = O/C–O-C and C(O)O bonds respectively, and the two peaks at 290.1 and 291.8 eV are

Table 1
Summarized specific surface areas, copper content, breakthrough time and capacity, and H_2S conversion of PCC, PCC-Cu and PCC-unleached.

Parameter/Property	Sample PCC	PCC-Cu	PCC-unleached
S_{BET} (m^2/g)	824	790	245
Copper content (wt.%)	(traces)	4.5	65
t_{bt} (min)	202	207	247
Capacity at t_{bt} (mmol/g)	3.332	3.347	4.069
H_2S Conversion (%)	32.24	23.79	17.80

shake-up satellite peaks due to final states where π-π^* transitions of the aromatic rings occurred in the photoemission process together with the emission of the photoelectrons. Fig. 7(c) presents the spectrum of the N1*s* core level region, where four contributions can be identified; C–Cu-N bonds give rise to the peak at a BE of 398.5 eV [37], pyrrolic-N is responsible for the contribution at 399.6 eV, while the signals at BEs of 401.0 and 402.7 eV are due to graphitic-N and oxidized N, respectively. Finally, in the XPS spectrum of the Cu2$p_{3/2}$ core level region in Fig. 7(d), the peak at a BE of 932.8 eV is attributed to metallic copper as well as to Cu-C-N bonds [37], the one at 935.1 eV is due to the CuO, and the one at 937.0 eV derives from the $Cu(OH)_2$. Lastly, the contributions at BEs above 940.0 eV represent satellite features of copper^{2+}.

The XPS spectra of PCC-unleached therefore clearly support the existence of the coordination network connecting carbon, copper, and nitrogen atoms, at the basis of the formation of the carbon cuboids [22].

2.2. H_2S removal study

The breakthrough curves that inform on the quantity of adsorbate that can be retained, were collected for each sample at 150 °C and are depicted in Fig. 8; a summary of the experimental values is presented in Table S1 in the Supporting Information. We noted that H_2S and SO_2 evolution, represented in Fig. 8 by the black and red line respectively, start concurrently and that the breakthrough curves do not show the typical S-shape typically observed for adsorption of one adsorbate. The breakthrough time, t_{bt}, was calculated as the time when the total concentration of the two sulfur-containing gases exceeds 5 ppm at the outlet; the t_{bt} and the calculated H_2S capacity at 5% for each of the samples, as well as the percentages of H_2S conversion, are shown in Table 1.

Conducting the sulfidation experiments on porous (PCC & PCC-Cu) and copper rich (PCC-unleached) materials, the expected behaviour is that of sorbents. When a sample acts as a sorbent, the recorded curve reaches at a certain time 100 ppm, which marks the point where the material starts to saturate and stops to adsorb. On the other hand, in the case of a perfect catalyst there would be no breakthrough and all of the gas would be transformed into elemental sulfur. After each experiment, a significant amount of elemental sulfur concentrated on the walls of the reactor between the sample and the exit is easily discernible (a photograph of the reactor right after the experiment for the PCC sample is shown in Fig. S2 as an example). This indicates that sulfur is produced during the reaction and that the three carbon powders do not act as only as sorbents but also as catalysts.

The sorption capability of all three compounds is significant: PCC and PCC-Cu both capture 3.3 mmol/g of hydrogen sulphide, and PCC-unleached 4.1 mmol/g (using a steady flow of H_2S the amount of moles adsorbed are recorded and the capacity is calculated as explained in Section 1.2.4). All three capacities are comparable with the ones of other carbon materials that contain copper already reported in literature, and sometimes even exceed them. A list of literature reported capacities and conditions are

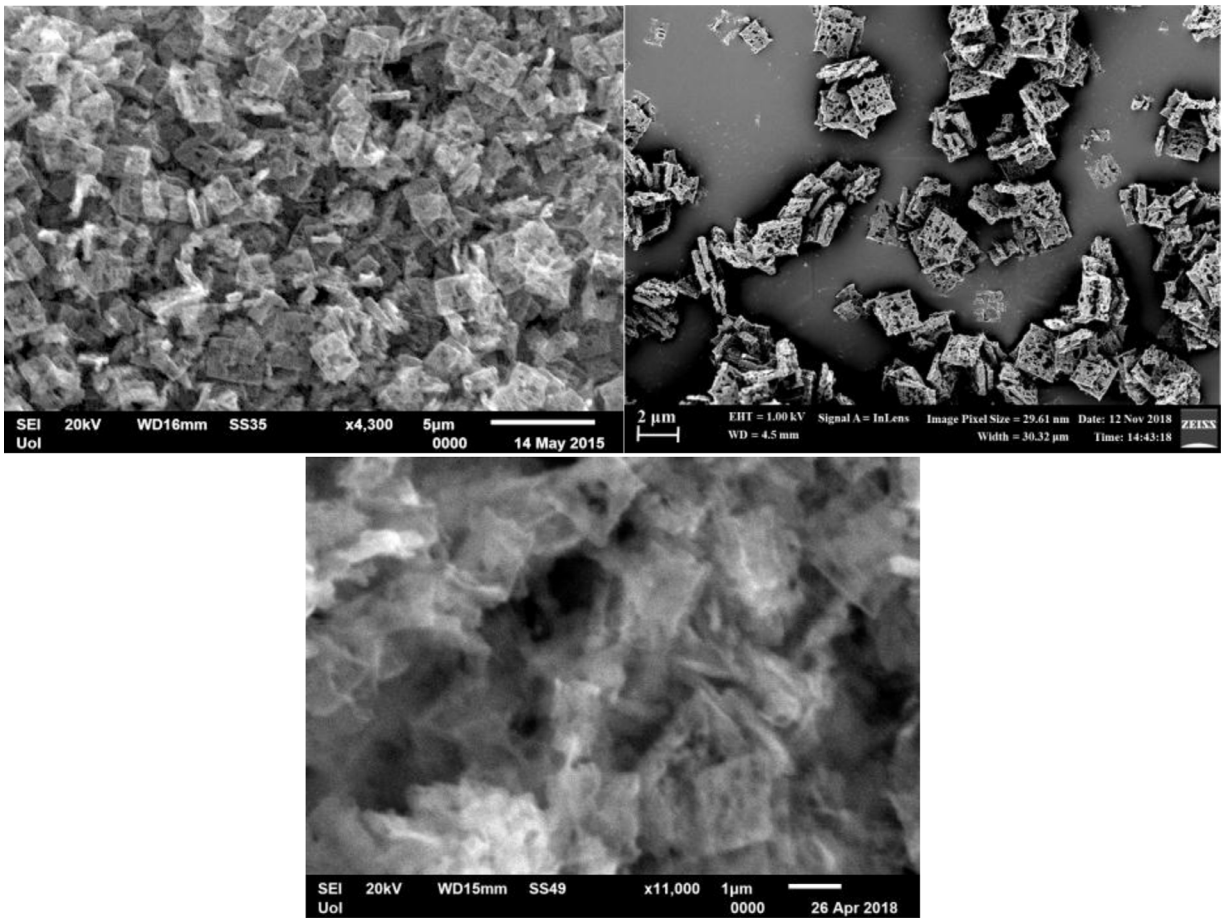

Fig. 4. Scanning electron microscopy images of PCC (top left, white bar = 5 μm), PCC-unleached (top right, white bar = 2 μm) and PCC-Cu (bottom, white bar = 1 μm).

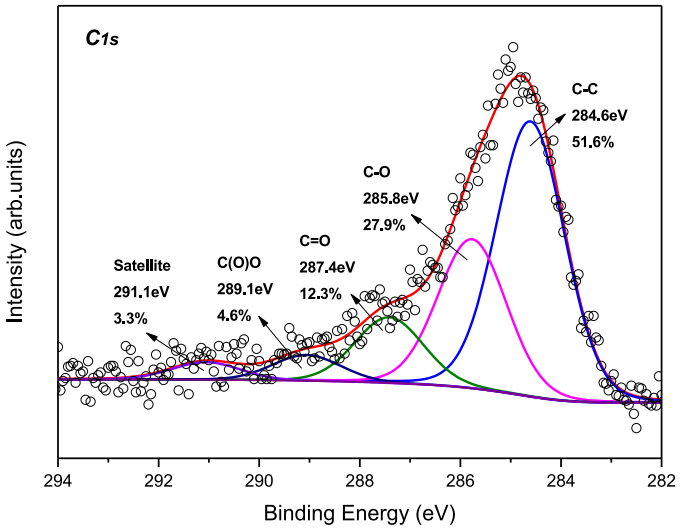

Fig. 5. XPS spectrum of the C1*s* core level region of PCC. The fit is also shown and for each component the binding energy together with the relative contribution to the total C1*s* spectral intensity are indicated.

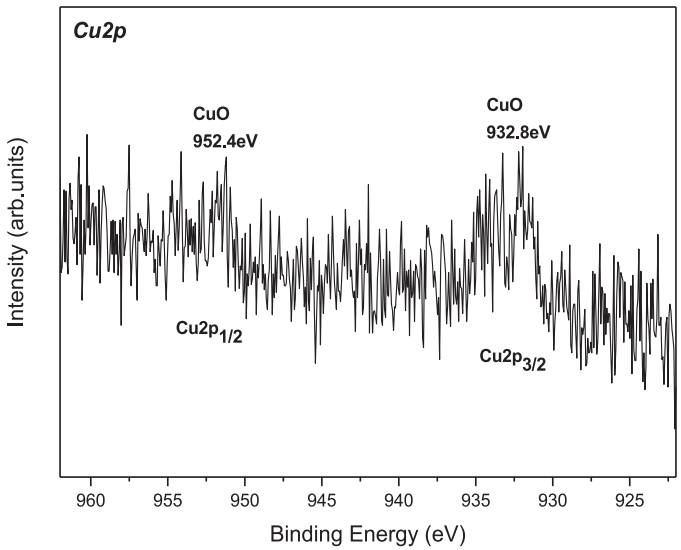

Fig. 6. XPS spectrum of the Cu2*p* core level region of PCC-Cu.

supplied as comparison in the Supplementary material (Table S2). PCC-unleached works better as a sorbent due to the higher amount of copper in the structure [38]. In the case of PCC, the absence of copper leads to lower capacity but higher conversion (~32%) due to the higher surface area. The breakthrough curves in the cases of PCC and PCC-Cu are less slanted since they act more as catalysts; the existence of more pores means that there are more pathways, which enhances the mass transfer. Finally, in the case of PCC-Cu, copper causes a partial blockage of the pores and hence a slightly lower surface area, which explains the lower conversion percentage (~23%), but at the same time the amount of Cu is not sufficient to increase the capacity, or the copper is not accessible to the H_2S.

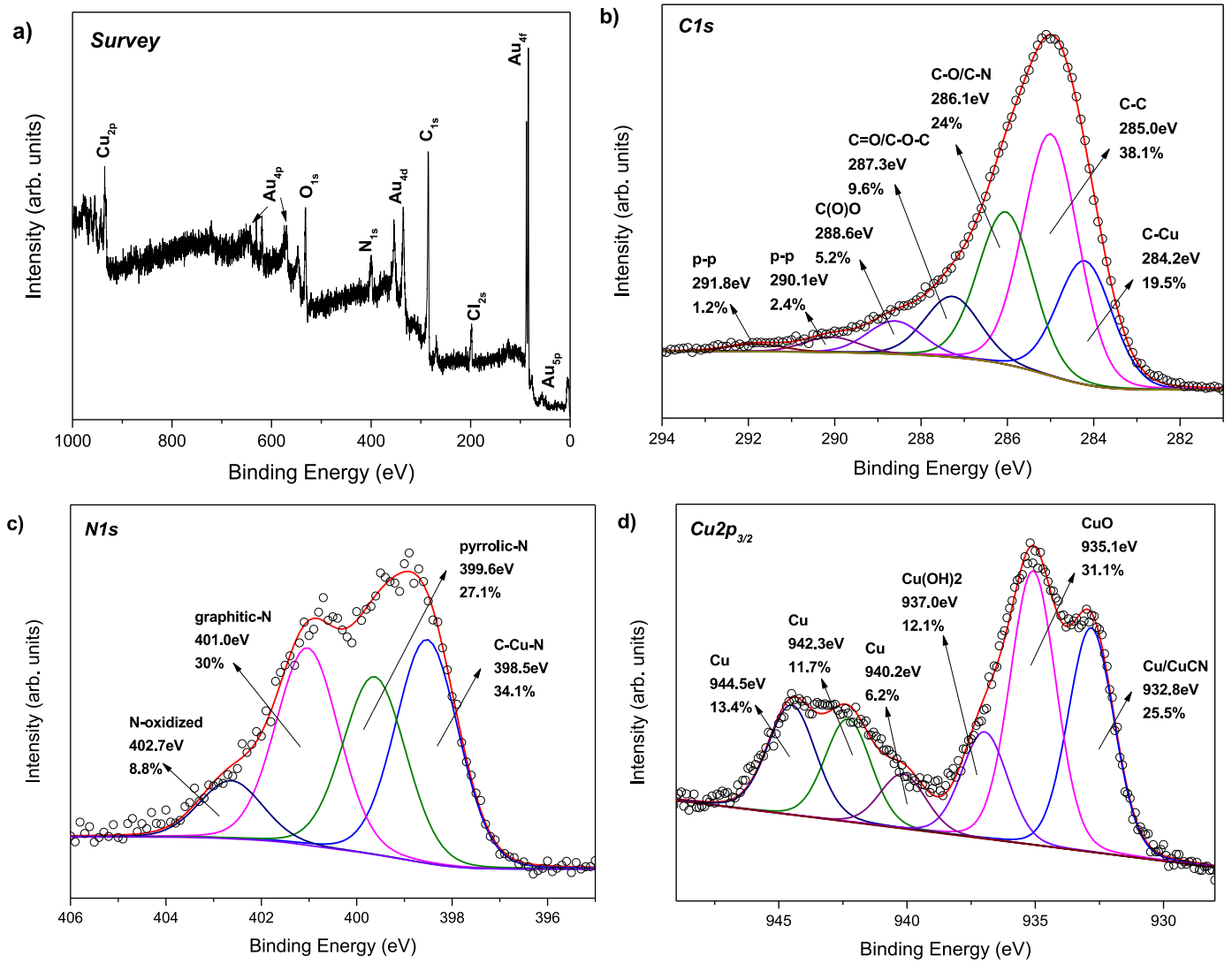

Fig. 7. XPS spectra of PCC-unleached: (a) survey scan, detailed spectra of the (b) C1*s*, (c) N1*s* and (d) Cu2*p* core level regions. For the detailed spectra the fit is also shown and for each component the binding energy together with the relative contribution to the total spectral intensity of the respective line are indicated.

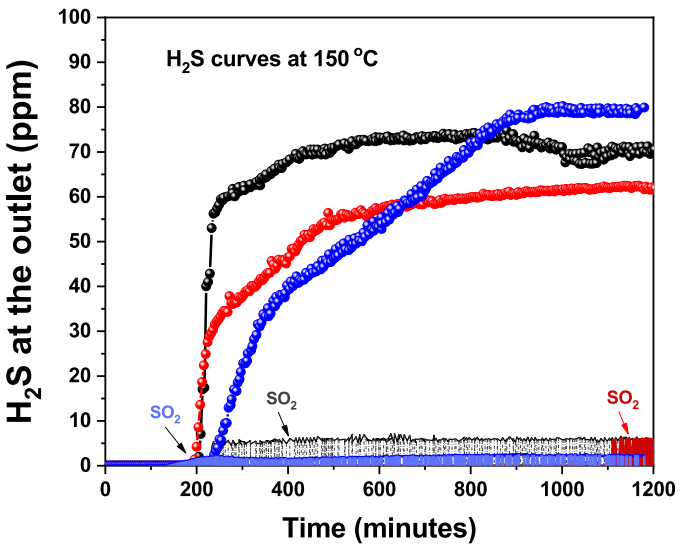

Fig. 8. Breakthrough curves of H_2S over PCC-unleached (blue), PCC (red) and PCC-Cu (black) after sulfidation at 150 °C. The SO_2 evolution for each sorbent is presented as well.

Hence for PCC and PCC-Cu, which both show a similar behaviour, the performance is credited to the porous matrix since in the first one there is no copper and in the latter the amount of Cu is calculated to be below 5 wt.%. Factors that might contribute to the good adsorptive behaviour are the nitrogen heteroatoms in the structure, which have been proven to enhance adsorption [1], or the presence of oxygen, which when part of the surface functional groups of activated carbon can promote oxidation reactions leading to elemental sulfur or other sulfur containing products that can participate in further reactions [39].

The accumulation of sulfur on all three porous carbon cuboids also decreases the active surface for adsorption and catalysis. With the evolution of the experiment, from a certain time onwards, H_2S can therefore no longer be totally adsorbed/consumed and this leads to saturation [40].

One notes that in none of the cases the breakthrough curves are completely smooth, as most evident in the case of PCC-Cu (Fig. 8), where bursts with an oscillating behaviour are seen. The reason for this behaviour is not clear but relevant literature reports that this phenomenon is observed whenever elemental sulfur is produced, accumulated on the catalyst, and cannot be removed from the reactor [41].

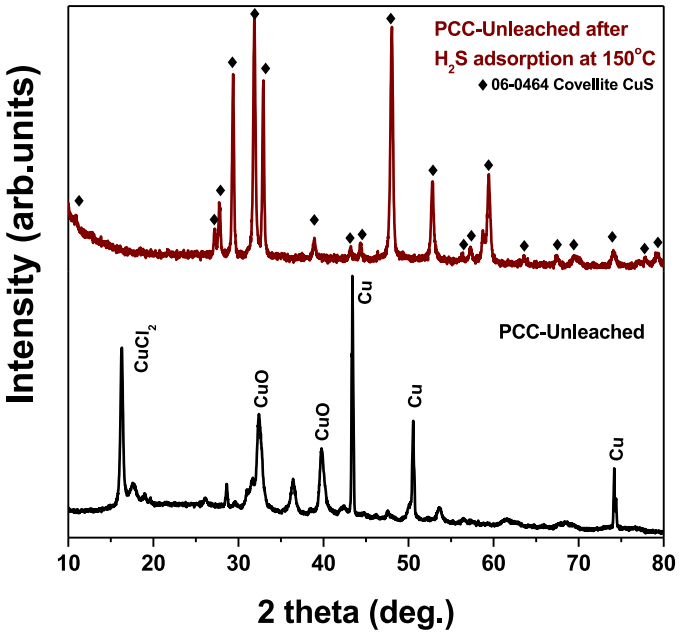

Fig. 9. Powder XRD patterns of the PCC-unleached sample, before and after sulfidation at 150 °C.

PCC-unleached was investigated a bit further because it has the highest sorption capacity despite its lower porosity, and presents a catalytic activity caused by carbon matrix and the presence of copper in various chemical environments.

It is clear that at least two reactions take place; as a first step, hydrogen sulfide is adsorbed onto the carbon matrix, then sulfidation of copper and selective oxidation of the gas occur to produce CuS and sulfur.

As mentioned in Section 1.3.1, copper in PCC-unleached is present in different forms: Cu-C-N bonds, metallic Cu, CuO and $CuCl_2$. After the H_2S experiment, the structure of the adsorbent-catalyst was again assessed *via* X-ray diffraction and the data are shown in Fig. 9 together with those of the initial PCC-unleached sample (remeasured right before the sulfidation process for better comparison). The peak at 36.5° can be attributed to Cu_2O (JCPDS card No. 01–078–2076), whereas the ones at 17.7, 28.6 and 53.6° could not be identified and may also be caused by impurities.

After the sulfidation experiment, the powder XRD pattern displays all the characteristic peaks of CuS (JCPDS card number of Covellite 06–0464, shown in Fig. S3 in the Supporting Information). This means that before the breakthrough time, when the adsorption is taking place, CuO is converted to CuS concurrently. Secondary reactions start to take place after the first three hours have passed, and as can be easily seen in Fig. 8, where the emission of SO_2 starts at that time. The concentration is low and SO_2 can be considered a by-product of the reactions taking place.

To learn whether these chemical reactions changed the morphological characteristics of PCC-unleached, we also collected SEM images after the sulfidation experiment. As seen in Fig. 10 no changes in the morphology of the sample can be identified (compare to Fig. 3 top right panel). The EDX results and the elemental mapping Table 1 and Fig. 10, respectively) confirm that a large amount of sulfur is present and well distributed all over the sample. The SEM elemental mapping and analysis of PCC-unleached before sulfidation are shown for comparison in Fig. 10 (top panel), and in Table 2, respectively Eqs. (2)–((5).

From the EDX analysis we calculated that the ratio of copper to sulfur atoms in the sample after sulfidation is almost 1:2, which justifies the presence of CuS as well as the emission of SO_2 and

Table 2
EDX analysis of PCC-unleached before and after sulfidation.

Element	Before wt.%	at.%	After wt.%	at.%
C	39.5	61.8	33.1	57.0
N	6.9	9.3	5.7	8.4
O	11.7	13.9	6.6	8.6
S	–	–	25.5	16.5
Cu	31.5	9.4	29.1	9.5
Cl	10.4	5.6	–	–

the production of elemental sulfur. It is noteworthy to mention that there is no chlorine detected after the sulfidation experiment; this proves that Cl has reacted with hydrogen sulfide leading to the production of sulfur [42].

2.3. Possible reactions – proposed mechanism

Based on experimental studies and theoretical calculations based on DFT [29,43–46], the reaction mechanism that leads to the conversion of H_2S to CuS can be explained by the following reaction steps:

Step 1: $H_2S + Cu\text{-}O \rightarrow H_2S \cdots Cu \cdots O$
Step 2: $H_2S \cdots Cu \cdots O \rightarrow HS\text{-}Cu + H\text{-}O$
Step 3: $HS\text{-}Cu + H\text{-}O \rightarrow CuS + H_2O$

In parallel, a redox (oxidation–reduction) reaction like the one shown here could be taking place:

$$H_2S + 3CuO \rightarrow H_2O + SO_2 + 3Cu$$

which would explain the emission of SO_2. CuO is an oxidizing and H_2S is a reducing agent:

$$3Cu^2 + 6e^- \rightarrow 3Cu^0(\text{reduction})$$

$$S^{-2} - 6e^- \rightarrow S^4(\text{oxidation})$$

Sulfur dioxide could in turn react with hydrogen sulfide, to produce elemental sulfur through the following redox reaction (H_2S is a reducing agent, SO_2 is an oxidizing agent):

$$SO_2(g) + 2H_2S(g) \rightarrow 2H_2O(l) + 3S(s)$$

$$2S^{-2} - 4e^- \rightarrow 2S^0(\text{oxidation})$$

$$S^4 + 4e^- \rightarrow S^0(\text{reduction})$$

In the case that a significant amount of oxygen was present during the experiment (possible leak or impurities in the H_2S gas from the provider), the reactions that take place when CuO is used for gas sensing applications [47–49], could also happen:

$$1/2O_2 + e^- \rightarrow O^-$$

$$3O^- + H_2S \rightarrow H_2O + SO_2 + 3e^-$$

$$CuO + H_2S \rightarrow CuS + H_2O$$

$$2CuS + 3O_2 \rightarrow 2CuO + 2SO_2$$

It has been proven that the presence of oxygen during hydrogen sulfide capture leads to the formation of elemental sulfur and sulfur dioxide, which can be enhanced by the presence of water

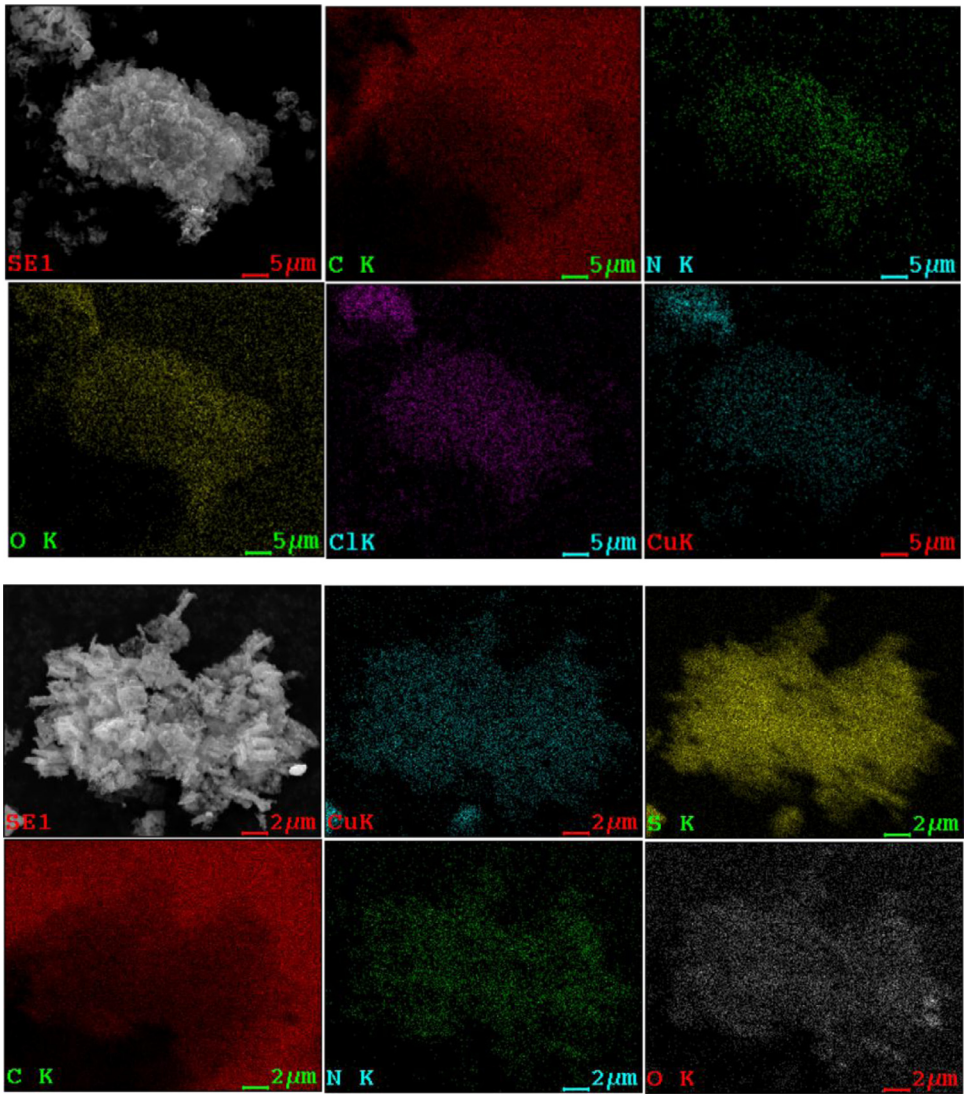

Fig. 10. SEM and elemental mapping of the PCC-unleached before (top) and after (bottom) sulfidation.

and can improve the adsorption process especially in sorbents that contain copper through the following reactions [10,39,50]:

$$1/2O_2 + H_2S \rightarrow S + H_2O$$

$$H_2S + 1.5O_2 \rightarrow SO_2 + H_2O$$

$$2H_2S + SO_2 \rightarrow 1/nS_n + H_2O$$

Hydrogen sulfide is partially oxidized to sulfur, and as the oxidation proceeds sulfur dioxide is also emitted, which is then consumed again by reacting with the gas to produce more sulfur [31].

Finally, other copper species (Cu_2O, $Cu(OH)_2$) present on the surface although not detected by XRD, might also have an important role and even be responsible for the sulfur production through their involvement in the reactions taking place. More specifically, Cu_2O can be converted to Cu_2S through sulfurization [51] and the chemical adsorption efficiency of copper hydroxide has already been reported in literature; it can react with hydrogen sulfide through the following reaction [52]:

$$Cu(OH)_2(s) + H_2S(g) \rightarrow CuS(s) + 2H_2O(g)$$

3. Conclusions

Three porous carbon cuboids with different characteristics were synthesized through carbonization of the product of a coordination reaction and their potential as H_2S sorbents was evaluated. The sorbents with the higher porosity showed lower sorption capacity and were also catalytically active. The copper-rich sample with the lowest surface area was proved to function also as a catalyst, with selective oxidation of hydrogen sulfide taking place. The latter was investigated a bit further and ideas about the potential mechanism behind the catalytic activity were put forward. Further improvement of the designed materials could lead in high performance catalysts suitable for H_2S conversion.

Declaration of Competing Interest

The authors declare that they have no known competing financial interests or personal relationships that could have appeared to influence the work reported in this paper.

CRediT authorship contribution statement

Eleni Thomou: Investigation, Formal analysis, Writing – original draft, Writing – review & editing. **Georgia Basina:** Inves-

tigation, Formal analysis, Validation, Writing – review & editing. **Konstantinos Spyrou:** Conceptualization, Investigation, Formal analysis, Validation, Supervision, Writing – review & editing. **Yasser Al Wahedi:** Formal analysis, Validation, Writing – review & editing. **Petra Rudolf:** Validation, Writing – review & editing, Supervision. **Dimitrios Gournis:** Conceptualization, Validation, Writing – review & editing, Supervision.

Acknowledgements

The authors would like to thank Dr. Christina Papachristodoulou, Dr. Vasilis Kostas, Jur van Dijken and Dr. Emmanuel P. Giannelis' group for assistance with the measurements. ET was financially supported by the Hellenic Foundation for Research and Innovation (HFRI) and the General Secretariat for Research and Technology (GSRT), under the HFRI PhD Fellowship grant (GA. No. 1829) and by the Ubbo Emmius programme of the University of Groningen.

Supplementary materials

Supplementary material associated with this article can be found, in the online version, at doi:.

References

[1] M. Khabazipour, M. Anbia, Removal of hydrogen sulfide from gas streams using porous materials: a review, Ind. Eng. Chem. Res. 58 (49) (2019) 22133–22164, doi:10.1021/acs.iecr.9b03800.
[2] A.D. Wiheeb, I.K. Shamsudin, M.A. Ahmad, M.N. Murat, J. Kim, M.R. Othman, Present technologies for hydrogen sulfide removal from gaseous mixtures, Rev. Chem. Eng. 29 (6) (2013) 449–470, doi:10.1515/revce-2013-0017.
[3] A.G. Georgiadis, N.D. Charisiou, M.A. Goula, Removal of hydrogen sulfide from various industrial gases: a review of the most promising adsorbing materials, Catalysts 10 (5) (2020) 521, doi:10.3390/catal10050521.
[4] E. Üresin, H.İ. Saraç, A. Sarıoğlan, Ş. Ay, F. Akgün, An experimental study for H_2S and CO_2 removal via caustic scrubbing system, Process Saf. Environ. Prot. 94 (2015) 196–202, doi:10.1016/j.psep.2014.06.013.
[5] M.S. Shah, M. Tsapatsis, J.I. Siepmann, Hydrogen sulfide capture: from absorption in polar liquids to Oxide, Zeolite, and Metal–organic framework adsorbents and membranes, Chem. Rev. 117 (14) (2017) 9755–9803, doi:10.1021/acs.chemrev.7b00095.
[6] O. Elmutasim, G. Basina, D.A. Shami, D. Gaber, S. Gaber, G.N. Karanikolos, Y.A. Wahedi, On the impact of copper local environment on hydrogen sulfide adsorption within microporous $AlPO_4$-5, J. Environ. Chem. Eng. 8 (5) (2020) 104245, doi:10.1016/j.jece.2020.104245.
[7] S.A. Nicolae, P.Á. Szilágyi, M.M. Titirici, Soft templating production of porous carbon adsorbents for CO_2 and H_2S capture, Carbon 169 (2020) 193–204, doi:10.1016/j.carbon.2020.07.064.
[8] C. Cara, E. Rombi, V. Mameli, A. Ardu, M. Sanna Angotzi, D. Niznansky, A. Musinu, C. Cannas, γ-Fe_2O_3-M41S Sorbents for H_2S removal: effect of different porous structures and silica wall thickness, J. Phys. Chem. C 122 (23) (2018) 12231–12242, doi:10.1021/acs.jpcc.8b01487.
[9] F. Rodríguez-Reinoso, A. Sepúlveda-Escribano, H.S. Nalwa, Chapter 9 - porous carbons in adsorption and catalysis, in: Handbook of Surfaces and Interfaces of Materials, Academic Press, Burlington, 2001, pp. 309–355.
[10] H.B. Fang, J.T. Zhao, Y.T. Fang, J.J. Huang, Y. Wang, Selective oxidation of hydrogen sulfide to sulfur over activated carbon-supported metal oxides, Fuel 108 (2013) 143–148, doi:10.1016/j.fuel.2011.05.030.
[11] B. Elyassi, Y.A. Wahedi, N. Rajabbeigi, P. Kumar, J.S. Jeong, X. Zhang, P. Kumar, V.V. Balasubramanian, M.S. Katsiotis, K. Andre Mkhoyan, N. Boukos, S.A. Hashimi, M. Tsapatsis, A high-performance adsorbent for hydrogen sulfide removal, Microporous Mesoporous Mater. 190 (2014) 152–155, doi:10.1016/j.micromeso.2014.02.007.
[12] L.J. Wang, H.L. Fan, J. Shangguan, E. Croiset, Z. Chen, H. Wang, J. Mi, Design of a sorbent to enhance reactive adsorption of hydrogen sulfide, ACS Appl. Mater. Interfaces 6 (23) (2014) 21167–21177, doi:10.1021/am506077j.
[13] O. Karvan, H. Atakül, Investigation of CuO/mesoporous SBA-15 sorbents for hot gas desulfurization, Fuel Process. Technol. 89 (9) (2008) 908–915, doi:10.1016/j.fuproc.2008.03.004.
[14] J.H. Yang, Hydrogen sulfide removal technology: a focused review on adsorption and catalytic oxidation, Korean J. Chem. Eng. 38 (4) (2021) 674–691, doi:10.1007/s11814-021-0755-y.
[15] X. Zheng, J. Cai, Y. Cao, L. Shen, Y. Zheng, F. Liu, S. Liang, Y. Xiao, L. Jiang, Construction of cross-linked δ-MnO_2 with ultrathin structure for the oxidation of H_2S: structure-activity relationship and kinetics study, Appl. Catal. B 297 (2021) 120402, doi:10.1016/j.apcatb.2021.120402.
[16] X. Zheng, Y. Li, Y. Zheng, L. Shen, Y. Xiao, Y. Cao, Y. Zhang, C. Au, L. Jiang, Highly efficient porous $Fe_xCe_{1-x}O_{2-\delta}$ with three-dimensional hierarchical nanoflower morphology for H_2S-selective oxidation, ACS Catal. 10 (7) (2020) 3968–3983, doi:10.1021/acscatal.9b05486.
[17] C. Duong-Viet, Y. Liu, H. Ba, L. Truong-Phuoc, W. Baaziz, L. Nguyen-Dinh, J.-.M. Nhut, C. Pham-Huu, Carbon nanotubes containing oxygenated decorating defects as metal-free catalyst for selective oxidation of H_2S, Appl. Catal. B 191 (2016) 29–41, doi:10.1016/j.apcatb.2016.03.018.
[18] G. Lei, Z. Dai, Z. Fan, X. Zheng, Y. Cao, L. Shen, Y. Xiao, C. Au, L. Jiang, Porous nanosheets of carbon-conjugated graphitic carbon nitride for the oxidation of H_2S to elemental sulfur, Carbon 155 (2019) 204–214, doi:10.1016/j.carbon.2019.08.052.
[19] G. Lei, Y. Cao, W. Zhao, Z. Dai, L. Shen, Y. Xiao, L. Jiang, Exfoliation of graphitic carbon nitride for enhanced oxidative desulfurization: a facile and general strategy, ACS Sustain. Chem. Eng. 7 (5) (2019) 4941–4950, doi:10.1021/acssuschemeng.8b05553.
[20] C. Xu, J. Chen, S. Li, Q. Gu, D. Wang, C. Jiang, Y. Liu, N-doped honeycomb-like porous carbon derived from biomass as an efficient carbocatalyst for H_2S selective oxidation, J. Hazard. Mater. 403 (2021) 123806, doi:10.1016/j.jhazmat.2020.123806.
[21] S. Li, Y. Liu, H. Gong, K.H. Wu, H. Ba, C. Duong-Viet, C. Jiang, C. Pham-Huu, D. Su, N-doped 3D mesoporous carbon/carbon nanotubes monolithic catalyst for H_2S selective oxidation, ACS Appl. Nano Mater. 2 (6) (2019) 3780–3792, doi:10.1021/acsanm.9b00654.
[22] G.P. Hao, G. Mondin, Z. Zheng, T. Biemelt, S. Klosz, R. Schubel, A. Eychmüller, S. Kaskel, Unusual ultra-hydrophilic, porous carbon cuboids for atmospheric-water capture, Angew. Chem. Int. Ed. 54 (6) (2015) 1941–1945, doi:10.1002/anie.201409439.
[23] J. Cui, Y. Yang, Y. Hu, F. Li, Rice husk based porous carbon loaded with silver nanoparticles by a simple and cost-effective approach and their antibacterial activity, J. Colloid Interface Sci. 455 (2015) 117–124, doi:10.1016/j.jcis.2015.05.049.
[24] A.K. Karumuri, D.P. Oswal, H.A. Hostetler, S.M. Mukhopadhyay, Silver nanoparticles supported on carbon nanotube carpets: influence of surface functionalization, Nanotechnology 27 (14) (2016) 145603, doi:10.1088/0957-4484/27/14/145603.
[25] D. Karageorgou, E. Thomou, N.T. Vourvou, K.-.M. Lyra, N. Chalmpes, A. Enotiadis, K. Spyrou, P. Katapodis, D. Gournis, H. Stamatis, Antibacterial and algicidal effects of porous carbon cuboid nanoparticles, ACS Omega 4 (3) (2019) 4991–5001, doi:10.1021/acsomega.8b02018.
[26] J.F. Moulder, W.F. Stickle, P.E. Sobol, Handbook of X-ray photoelectron spectroscopy: a reference book of standard spectra for identification and interpretation of XPS data, Physical Electronics, Inc., Eden Prairie, Minn., 1995.
[27] S.M. Mendoza, Exploiting Molecular Machines on Surfaces, University of Groningen, 2007.
[28] D.A. Shirley, High-resolution X-Ray photoemission spectrum of the valence bands of gold, Phys. Rev. B 5 (12) (1972) 4709–4714, doi:10.1103/PhysRevB.5.4709.
[29] G. Basina, D.A. Gaber, S.A. Yafei, V. Tzitzios, S.A. Gaber, I. Ismail, B.V. Vaithilingam, K. Polychronopoulou, S.A. Hashimi, Y.A. Wahedi, Mesoporous silica "plated" copper hydroxides/oxides heterostructures as superior regenerable sorbents for low temperature H_2S removal, Chem. Eng. J. 398 (2020) 125585, doi:10.1016/j.cej.2020.125585.
[30] M.A. Haija, G. Basina, F. Banat, A.I. Ayesh, Adsorption and gas sensing properties of CuFeO nanoparticles, Mater. Sci. Poland 37 (2) (2019) 289–295, doi:10.2478/msp-2019-0020.
[31] G. Basina, O. Elmutasim, D.A. Gaber, S.A. Gaber, X. Lu, V. Tzitzios, B.V. Vaithilingam, M. Baikousi, G. Asimakopoulos, M.A. Karakassides, I. Panagiotopoulos, K. Spyrou, E. Thomou, E. Sakellis, N. Boukos, D. Xu, M. Tsapatsis, N.A. Amoodi, Y.A. Wahedi, On the selective oxidation of H_2S by heavy loaded nanoparticles embedded in mesoporous matrix (NEMMs), Appl. Catal. B 278 (2020) 119338, doi:10.1016/j.apcatb.2020.119338.
[32] A.V. Chatzikonstantinou, E. Gkantzou, E. Thomou, N. Chalmpes, K.-.M. Lyra, V.G. Kontogianni, K. Spyrou, M. Patila, D. Gournis, H. Stamatis, Enzymatic conversion of oleuropein to hydroxytyrosol using immobilized β-glucosidase on porous carbon cuboids, Nanomaterials 9 (8) (2019) 1166, doi:10.3390/nano9081166.
[33] D. Collins, T. Luxton, N. Kumar, S. Shah, V.K. Walker, V. Shah, Assessing the impact of copper and zinc oxide nanoparticles on soil: a field study, PLoS One 7 (8) (2012) e42663, doi:10.1371/journal.pone.0042663.
[34] L. Zhong, W. Ruiyu, Z. Huayan, X. Kechang, Preparation of CuIY catalyst using $CuCl_2$ as precursor for vapor phase oxidative carbonylation of methanol to dimethyl carbonate, Fuel 89 (7) (2010) 1339–1343, doi:10.1016/j.fuel.2009.10.021.
[35] V.N. Daggupati, G.F. Naterer, K.S. Gabriel, R.J. Gravelsins, Z.L. Wang, Equilibrium conversion in Cu–Cl cycle multiphase processes of hydrogen production, Thermochim. Acta 496 (1) (2009) 117–123, doi:10.1016/j.tca.2009.07.009.
[36] K. Spyrou, M. Calvaresi, E.A.K. Diamanti, T. Tsoufis, D. Gournis, P. Rudolf, F. Zerbetto, Graphite oxide and aromatic amines: size matters, Adv. Funct. Mater. 25 (2) (2015) 263–269, doi:10.1002/adfm.201402622.
[37] R.C. Dante, F.M. Sánchez-Arévalo, P. Chamorro-Posada, J. Vázquez-Cabo, L. Huerta, L. Lartundo-Rojas, J. Santoyo-Salazar, O. Solorza-Feria, A. Diaz-Barrios, T. Zoltan, F. Vargas, T. Valenzuela, F. Muñoz-Bisesti, F.J. Quiroz-Chávez, Synthesis and characterization of Cu-doped polymeric carbon nitride, Fuller. Nanotub. Carbon Nanostruct. 24 (3) (2016) 171–180, doi:10.1080/1536383X.2015.1124864.
[38] D. Nguyen-Thanh, T.J. Bandosz, Activated carbons with metal containing ben-

tonite binders as adsorbents of hydrogen sulfide, Carbon 43 (2) (2005) 359–367, doi:10.1016/j.carbon.2004.09.023.
[39] S. Cimino, L. Lisi, A. Erto, F.A. Deorsola, G. de Falco, F. Montagnaro, M. Balsamo, Role of H_2O and O_2 during the reactive adsorption of H_2S on CuO-ZnO/activated carbon at low temperature, Microporous Mesoporous Mater. 295 (2020) 109949, doi:10.1016/j.micromeso.2019.109949.
[40] E. Laperdrix, G. Costentin, O. Saur, J.C. Lavalley, C. Nédez, S. Savin-Poncet, J. Nougayrède, Selective oxidation of H_2S over CuO/Al_2O_3: identification and role of the sulfurated species formed on the catalyst during the reaction, J. Catal. 189 (1) (2000) 63–69, doi:10.1006/jcat.1999.2691.
[41] O.N. Kovalenko, N.N. Kundo, V.M. Novopashina, V.M. Khanaev, Investigation of H_2S oxidation by oxygen on oxide catalysts in sulfur condensation conditions, React. Kinet. Catal. Lett. 64 (1) (1998) 129–137, doi:10.1007/BF02475380.
[42] M.H. Khundkar, M. Rakiboddowla, Reaction between chlorine and hydrogen sulphide over alumina catalyst, J. Appl. Chem. 5 (2) (1955) 75–81, doi:10.1002/jctb.5010050207.
[43] Z. Li, N. Wang, Z. Lin, J. Wang, W. Liu, K. Sun, Y.Q. Fu, Z. Wang, Room-temperature high-performance H_2S sensor based on porous cuo nanosheets prepared by hydrothermal method, ACS Appl. Mater. Interfaces 8 (32) (2016) 20962–20968, doi:10.1021/acsami.6b02893.
[44] J.A. Rodriguez, T. Jirsak, M. Pérez, S. Chaturvedi, M. Kuhn, L. González, A. Maiti, Studies on the behavior of mixed-metal oxides and desulfurization: reaction of H_2S and SO_2 with Cr_2O_3(0001), MgO(100), and $Cr_xMg_{1-x}O$(100), J. Am. Chem. Soc. 122 (49) (2000) 12362–12370, doi:10.1021/ja003149j.
[45] F. Peng, Y. Sun, Y. Lu, W. Yu, M. Ge, J. Shi, R. Cong, J. Hao, N. Dai, Studies on sensing properties and mechanism of CuO nanoparticles to H_2S Gas, Nanomaterials 10 (4) (2020) 774, doi:10.3390/nano10040774.
[46] S. Yasyerli, G. Dogu, I. Ar, T. Dogu, Activities of copper oxide and Cu−V and Cu−Mo mixed oxides for H_2S removal in the presence and absence of hydrogen and predictions of a deactivation model, Ind. Eng. Chem. Res. 40 (23) (2001) 5206–5214, doi:10.1021/ie0010621.
[47] G.E. Patil, D.D. Kajale, S.D. Shinde, V.G. Wagh, V.B. Gaikwad, G.H. Jain, S.C. Mukhopadhyay, K.P. Jayasundera, A. Fuchs, Synthesis of Cu-Doped SnO_2 thin films by spray pyrolysis for gas sensor application, in: Advancement in Sensing Technology: New Developments and Practical Applications, Springer Berlin Heidelberg, Berlin, Heidelberg, 2013, pp. 299–311, doi:10.1007/978-3-642-32180-1_17.
[48] S. Navale, M. Shahbaz, S.M. Majhi, A. Mirzaei, H.W. Kim, S.S. Kim, CuxO nanostructure-based gas sensors for H_2S detection: an overview, Chemosensors 9 (6) (2021) 127, doi:10.3390/chemosensors9060127.
[49] Z. Huang, X. Wang, F. Sun, C. Fan, Y. Sun, F. Jia, G. Yin, T. Zhou, B. Liu, Super response and selectivity to H_2S at room temperature based on CuO nanomaterials prepared by seed-induced hydrothermal growth, Mater. Des. 201 (2021) 109507, doi:10.1016/j.matdes.2021.109507.
[50] R. Sitthikhankaew, D. Chadwick, S. Assabumrungrat, N. Laosiripojana, Effects of humidity, O_2, and CO_2 on H_2S adsorption onto upgraded and KOH impregnated activated carbons, Fuel Process. Technol. 124 (2014) 249–257, doi:10.1016/j.fuproc.2014.03.010.
[51] P. Zhang, H. Zhu, K. Xue, L. Chen, C. Shi, D. Wang, J. Li, X. Wang, G. Cui, H_2S detection at low temperatures by Cu_2O/Fe_2O_3 heterostructure ordered array sensors, RSC Adv. 10 (14) (2020) 8332–8339, doi:10.1039/C9RA10054G.
[52] D.A. Giannakoudakis, M. Jiang, T.J. Bandosz, Highly efficient air desulfurization on self-assembled bundles of copper hydroxide nanorods, ACS Appl. Mater. Interfaces 8 (46) (2016) 31986–31994, doi:10.1021/acsami.6b10544.